Draft version October 16, 2023
Typeset using LaTeX **twocolumn** style in AASTeX631

Spectroscopy of Ni I and Ni II in the Ultraviolet and Visible Regions

B. R. Neff,[1] S. J. Bromley,[2] D. A. Ennis,[2] G. J. Hartwell,[2] D. A. Maurer,[2] S. D. Loch,[2] C. A. Johnson,[2,3] and J. P. Marler[1]

[1] *Department of Physics and Astronomy, Clemson University, Clemson, SC 29634, USA*
[2] *Department of Physics, Auburn University, Auburn, AL 36849, USA*
[3] *Oak Ridge National Lab, Oak Ridge, TN 37830, USA*

ABSTRACT

Identification and characterization of nickel emission is important to our understanding in several areas of astrophysics, including studies of solar abundances. Laboratory studies of nickel emission provide important parameters for interpreting astrophysical spectra in the form of accurate wavelengths, and contributions of different excitation pathways to observed emission features. We report here an analysis of UV/VIS spectra for Ni I and Ni II obtained the Compact Toroidal Hybrid (CTH) plasma experiment at Auburn University. The nickel spectra were collected between 200 nm and 800 nm from high-temperature ($T_{\rm e} \sim 30$ eV) plasma erosion of a nickel-plated stainless steel probe inserted into the CTH. In total, 205 lines from Ni I were observed, 108 of which are unreported in literature, and twenty Ni II lines, of which three are previously unreported. The confirmed line identifications include sixteen lines from the recent publication by C. Clear on the spectrum of Ni II. Tentative identifications, based on the Ritz wavelengths computed from known level energies, comparisons of multiple probe datasets from previous CTH experiments, and collisional-radiative models incorporating electron impact excitation data are reported. The data are used to propose benchmarks for R-matrix electron impact data recently reported in literature. A comparison between the observed spectrum and a collisional-radiative model reveals comparable distributions of emission features in the UV region. A Ni II line ratio of two strong observed lines at 231.60 nm and 241.62 nm is used to showcase the sensitivity to plasma conditions and motivate further benchmarking studies.

1. INTRODUCTION

Determining accurate stellar abundances of various elements, especially those in the iron group, plays an important role in addressing fundamental questions about the formation of our solar system. Within the iron-group, second in abundance to iron is atomic nickel (Z = 28; $\log_{10}$(Ni/Fe) = -1.1). Previous work has been done to analyze the solar abundance of Ni I by Asplund et al. (2009), as well as Ni II by Grevesse & Swings (1970). Typically, abundances are derived from spectral features for which accurate laboratory data, e.g. experimentally-measured transition rates and wavelengths, are available. Deriving abundances from Ni II features is particularly difficult due to a combination of insufficient atomic data and weak lines in solar spectra.

The laboratory studies that underpin measurements of solar Ni abundance extend back many decades, with some details available as far back as 1919 (Meggers & Kiess 1919). In the latter half of the 20$^{\text{th}}$ century, the analyses of Meggers et al. (1975), Shenstone (1970), Huber & Sandeman (1980), and Wickliffe & Lawler (1997) greatly extended the data for both classified transitions and transition rates needed to derive stellar abundances. Meggers et al. (1975) studied the spectrum of Ni I produced by an arc source between 200 - 900 nm. Shenstone (1970) utilized a hollow cathode to excite transitions of Ni II between 70 - 1000 nm. Huber & Sandeman (1980) derived transition rates and branching fractions for many transitions of Ni I using the Hook method. Wickliffe & Lawler (1997) used hollow cathode lamp spectra taken from the archives of the National Solar Observatory to study branching fractions and atomic transition probabilities for Ni I. With the exception of the arc source in Meggers et al. (1975), these environments are relatively low-temperature ($T_{\rm e} \leq 5$ eV). Comparison of the line lists in these works show relatively weak intensities for transitions from the more highly-excited levels. Most recently, Ni II received a detailed analysis of its emission, with many singly-excited configurations of the form $3d^8 n\ell$ identified by Clear et al. (2022). Using both grating and Fourier transform spectroscopy, Clear et al. (2022) reported a comprehensive list of lines and levels derived from observed features emitted from a nickel-helium hollow cathode lamp between 0.15 and 5.5 μm.

As noted above, the wavelengths of Ni emission features excited in low-temperature laboratory plasmas are well characterized. At higher temperatures ($T_{\rm e} \geq 30$ eV), however, highly-excited states may be efficiently populated. Additionally, the typical electron densities in higher-density plasmas ($n_{\rm e} \geq 10^{12}$ cm^{-3}) are likely insufficient to maintain LTE, in particular for d-shell elements which may contain many metastable levels. For example, Bromley et al. (2020) recently reported Au I and Au II emission lines observed from erosion of a gold-plated probe in a high-temperature ($T_{\rm e} \sim 30$ eV) plasma at the Compact Toroidal Hybrid (CTH) facility. The analysis conducted by Bromley et al. (2020) relied on comparison of spectra collected from erosion of two plated probes: 1) a stainless steel probe coated with gold, and 2) a stainless steel probe coated in nickel. The identifications in Bromley et al. (2020) relied on existing high-resolution wavelength data for both Au I and Au II, resulting in the tentative identifications of many lines driven by excitation from metastable levels. Collisional-radiative emission modeling of Au I in McCann et al. (2021) showed that at these plasma conditions, metastable populations are far from LTE, and many of the strongest emission lines are sensitive to the metastable level populations. Similar trends are expected in Ni ions, owing to the open $3d$ shell, but have until now remained largely unexplored.

In Bromley et al. (2021), the CTH datasets were used to identify features of atomic nickel and iron and in the coma of comet C/1996 B2 (Hyakutake). When excited by solar fluorescence, the emission of Ni and Fe atoms primarily results from ultraviolet/visible decays of low-lying excited states pumped by metastable levels. As a result, the Ni and Fe lines identified in Bromley et al. (2021) relied on the decades-long literature of high-resolution wavelength measurements conducted in low-temperature laboratory plasmas. When compared to Ni/Fe emission from tenuous cometary atmospheres, laboratory plasmas are likely to exhibit many more transitions, owing to the typically-Maxwellian distribution of electron energies. In particular, high-temperature laboratory plasmas are more likely to populate highly-excited states which may not be easily observed in low-temperature discharges. This was demonstrated in Johnson et al. (2019b), which utilized a similar experimental setup in the CTH to study the ultraviolet emission of tungsten. We report here a deeper analyses of the CTH nickel probe data, previously described in Bromley et al. (2021) and Bromley et al. (2020), and report the sum total of Ni I and Ni II emission features available in these archived datasets. In the course of the analysis, we utilized all available nickel/gold CTH data, as well as data from CTH experiments with tungsten and molybdenum probes, to support the line identifications.

The conditions in CTH discharges, i.e. electron temperatures of order 10 - 40 eV and electron densities of order 10^{12} cm^{-3}, place the excitation conditions firmly within the collisional-radiative regime, where level populations and radiative transition intensities are determined by the balance of collisional excitation, collisional de-excitation, and spontaneous emission, and a full solution of the time-dependent metastable-resolved kinematic equations may be required. We note that though these measurements are carried out at a lower wavelength resolution than typical stellar or high-resolution laboratory measurements, and hence the wavelength accuracies of these line lists are insufficient for e.g. identification of lines in stellar spectra, the plasma conditions in the CTH provide a unique opportunity to benchmark theoretical electron-impact excitation data. To that end, the purpose of this paper is to confirm spectral line identifications of Ni I and Ni II in a high-temperature plasma experiment, and provide preliminary benchmarking for theoretical electron impact data.

Our manuscript proceeds as follows. In Section 2, an overview of the experimental campaign and plasma apparatus used to excite the observed nickel emission features is provided. Section 3 details the procedures used to analyze the numerous nickel probe datasets. Section 4 provides a complete account of the observed transitions, comments on the electronic structures of Ni I and Ni II and their impact on the observed emission, and considerations for future collisional-radiative modeling efforts. A summary of the work is included in Section 5.

2. EXPERIMENT

Detailed accounts of the experimental apparatus and analysis procedures are provided in Hartwell et al. (2017), Johnson et al. (2019b), and Bromley et al. (2020). A brief summary is provided here. The Compact Toroidal Hybrid (CTH) apparatus at Auburn University is a hybrid stellarator/tokamak device used to study magnetohydrodynamic instabilities in current-carrying plasmas. In the present work, spectra were collected from the plasma interaction with a nickel-plated probe inserted at a distance of 19.9, 22.9, or 25.9 cm from the midplane of the CTH. At 25.9 cm, the probe is near or outside of the last closed flux surface of the plasma, and therefore we expect very little interaction between the probe and plasma at this position. Each discharge is initiated by microwave heating, producing a plasma with an electron temperature of $T_{\rm e}$ ∼5 eV and density $n_{\rm e} \sim 10^{11}$ cm^{-3} at the midplane. In the latter half of the discharge, the core temperature is increased to $T_{\rm e} \leq 150$ eV with $n_{\rm e} \sim 10^{13}$ cm^{-3} by driving a plasma current with an ohmic heating coil; however, the plasma conditions in the edge are significantly lower. During experiments to investigate tungsten emission under similar plasma conditions, Johnson et al. (2023) inferred the electron temperature to be in the range of 15 to 35 eV at

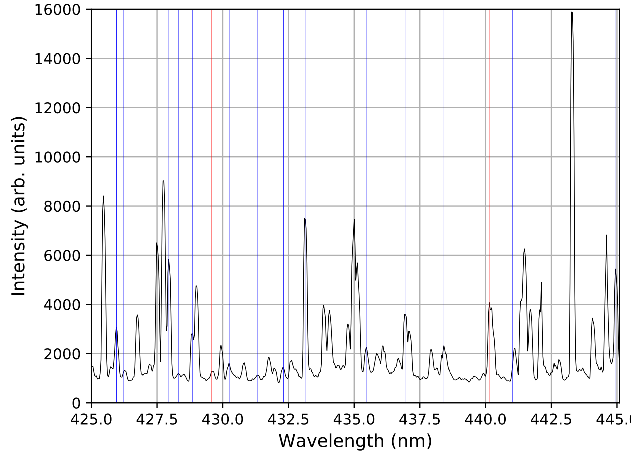

Figure 1. Sample spectra taken with the nickel probe at 22.9 cm (CTH shot #18112918). Vertical lines show the positions of known Ni I lines (red) and newly identified Ni I lines (blue).

the probe location during the current-carrying portion of the discharge.

On the underside of the CTH vacuum vessel, UV-optimized collection optics guide emission originating from the probe surface and along the line of sight into an optical fiber which is connected to the entrance slit of a Princeton Instruments HRS 500 monochromator operating at a data acquisition rate of 800 Hz. A 1200 g/mm grating yielded spectral windows approximately 40 nm wide with a resolving power $\sim 5 \times 10^3$ for each grating angle. In total, 17 different discharges were needed to observe the entire wavelength range. During typical plasma discharges, the ohmic coil drove current for approximately 50 ms, leading to at most 40 spectra during the high-temperature portion of the discharge. Wavelength calibration is achieved by observation of Hg/Ar/Ne lamps using Princeton Instrument's IntelliCal software. No intensity calibration was applied.

3. ANALYSIS

Each spectrum was analyzed as follows. The raw spectra are first processed to remove contamination of x-rays striking the spectrometer CCD (Bromley et al. 2020). For each time slice of a given discharge, the locations of the spectral peaks are identified by an automated peak-finding algorithm, a central wavelength is extracted from a Gaussian fit to the lines in each time slice, and the intensity value is recorded. A sample of a processed spectrum is shown in Fig. 1; vertical bars indicate previously-known lines (red) and newly-identified lines (blue, discussed below). Spectra were not taken at all wavelength ranges for a probe depth of 19.9 cm, and thus wave-

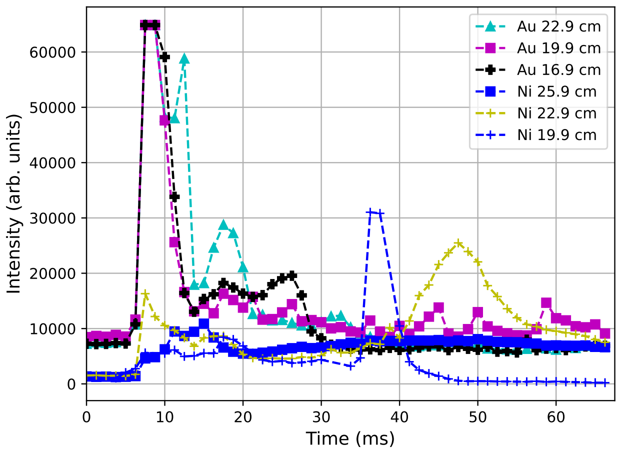

Figure 2. Intensity of the 486.15 nm Hydrogen I line over a 50 ms interval starting when the ohmic heating coils are fired (shot numbers in descending legend order: 18112745, 18112759, 18112765, 18112910, 18112922, 18112942). As H is the working gas, H I emission is present in every discharge.

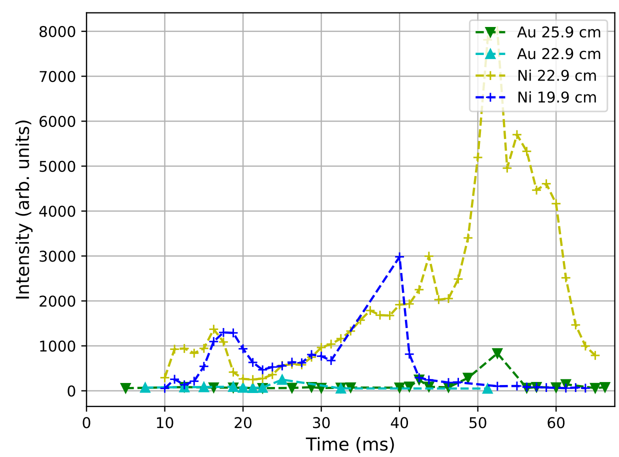

Figure 3. Intensity of the 427.95 nm Ni I ($3d^8 4s5s \rightarrow 3d^8 4s4p$) line over a 50 ms interval starting when the ohmic heating coils are fired (shot numbers in descending legend order: 18112722, 18112743, 18112920, 18112939). The Ni I transition(s) are absent from the Au dataset, and show a similar temporal evolution in both 22.9 cm and 19.9 cm Ni probe discharges. Truncation of the emission around 40 ms in the Ni probe 19.9 cm data is caused by plasma disruption and loss of plasma containment.

lengths of Ni lines are taken from the 22.9 cm spectra, with their presence in the spectra confirmed using the data from 19.9 cm probe depth where available. The wavelength scales were calibrated using Hg and Ne/Ar lamps and the IntelliCal software, resulting in a wavelength uncertainty of ±0.05 nm. The statistical uncer-

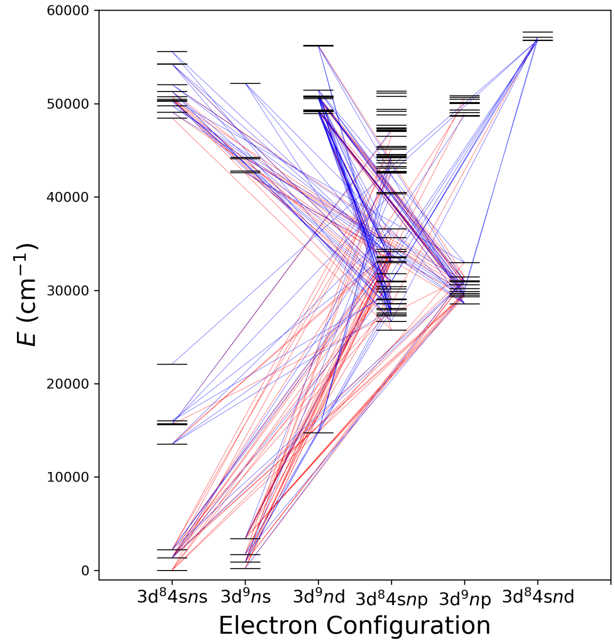

Figure 4. Grotrian diagram of Ni I. Only configurations with experimentally identified emission features are shown. Diagonal lines are shown for each observed transition. Transitions previously identified in literature are shown in red, with new lines shown in blue.

tainty, typically ≤0.04 nm, is computed as the standard deviation of the central wavelength across all detections of the feature in the 22.9 cm probe-depth nickel spectra. A final uncertainty is computed as the quadrature sum of the statistical uncertainty and the uncertainty of the wavelength calibration (~ 0.06 nm).

To identify an observed emission feature as nickel, comparisons are made to spectral data from CTH experiments which analyzed other elements under similar conditions. The nickel spectra analyzed in this work were compared to molybdenum and tungsten spectra from Johnson (2020). Any emission features appearing in the spectra taken with tungsten or molybdenum probes were determined to not be nickel emission. Confirmation of a nickel feature is also aided by "intensity-scatter plots" utilizing spectra from the nickel and gold CTH campaigns. A peak-finding algorithm is used to track the time evolution of each spectral feature in a given discharge. Figure 2 shows the time-evolution of the $n = 4 \rightarrow n = 2$ Balmer line of H I. The time scale used here and in the rest of this work is such that $t = 0$ ms when the ohmic heating coils are fired. Hydrogen is injected into the machine at the beginning of each discharge, and H I lines are present at nearly all times

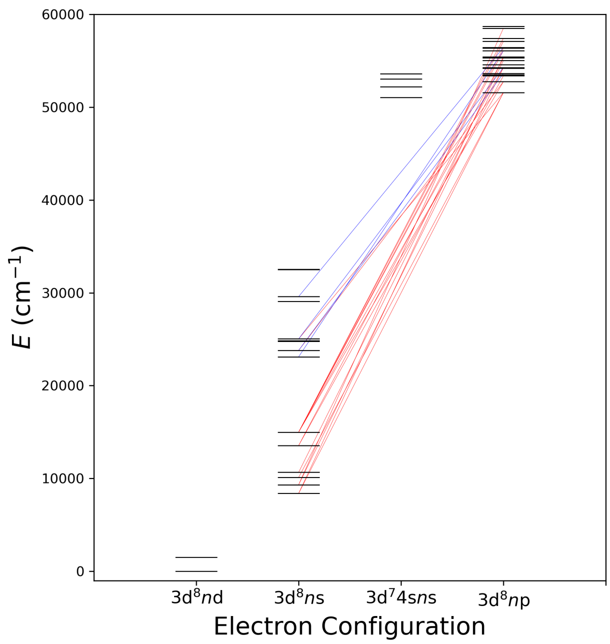

Figure 5. Grotrian diagram of Ni II. Known lines are shown in red, and newly identified lines are shown in blue.

in both the current-free and current-carrying phases of the discharges. In contrast, features of Ni I show a different behaviour as a function of time. Figure 3 shows the time-dependence of the 427.95 nm Ni I line. Nickel is eroded into the plasma, with line intensities peaking during the hottest portions of the (current-carrying) discharges. The line may be immediately attributed to nickel as the line is not observed in the gold probe spectrum, and shows a marked increase in emission during the portion of the discharge with highest plasma current.

The final determination on the emitting species (H, C, N, O, Ni, ...) is made by comparing the wavelengths of spectral features with suitable time-dependence to those of known lines. To confirm a line as Ni I or Ni II, it is required that the line's emission be absent in the Au, W, and Mo probe data. Additionally, the line must be present in the 22.9 cm and 19.9 cm probe depth data, and weak or absent from the 25.9 cm spectrum. The list of lines with suitable time-dependent behaviour is compared against the literature to confirm identification. Using the level information in the NIST Atomic Spectra Database (ASD) (Kramida et al. 2020), a list of electric dipole-allowed transitions was generated. Lines which match within the statistical wavelength uncertainty (0.04 nm) are reported as Ni I or Ni II.

Table 3 shows the number of transitions observed from different upper level electron configurations. All observed transitions of Ni I and Ni II are shown in Tables 2 and 3, respectively. Each wavelength range observed by the spectrometer is indicated by horizontal lines, with each range observed in separate but similar discharges; thus comparisons of observed intensities should only be made for lines close together within a single wavelength window. Intensities are reported using a procedure similar to that of Bromley et al. (2020). For a particular wavelength window, one frame is used to find the integrated intensities of all emission lines. However, given that the plasma conditions are not identical for all discharges, the same frame is not used across all wavelength windows. Intensities are normalized such that the strongest line in each wavelength window has an intensity of 100. Note that the intensities are not corrected for instrument sensitivity and losses in the optical elements. Thus, the relative intensities given in Tables 2 and 3 have an unmeasured source of uncertainty due to differences in the response of the optics and detector as a function of wavelength.

In Tables 2 and 3, both the level indices (energy order) and level energies are reported, with details of the energy levels in Ni I and Ni II provided in the supplementary materials. Ritz wavelengths were calculated from the available level energies and converted to air wavelengths using the conversion from Morton (2000); both the Ritz wavelengths and the difference between Ritz and observed wavelengths are provided.

Table 1. Summary of Observed Ni I Transitions From Different Upper Level Configurations

Configuration	Number of transitions
$3d^84sns$	28
$3d^9ns$	11
$3d^9n$d	63
$3d^8nsnp$	50
$3d^9np$	22
$3d^8nsn$d	13

4. DISCUSSION

Using the procedures described in Sec. 3, we identified two-hundred and five (205) transitions belonging to Ni I, and twenty (20) lines of Ni II within our accessed wavelength window of 200 - 800 nm. To the best of the author's knowledge, one-hundred and eight (108) transitions of Ni I are identified for the first time here. In Ni II, three lines are reported for the first time. The importance of each is discussed in turn.

A Grotrian diagram of Ni I is shown in Fig. 4. In this plot, transitions previously reported in the literature are

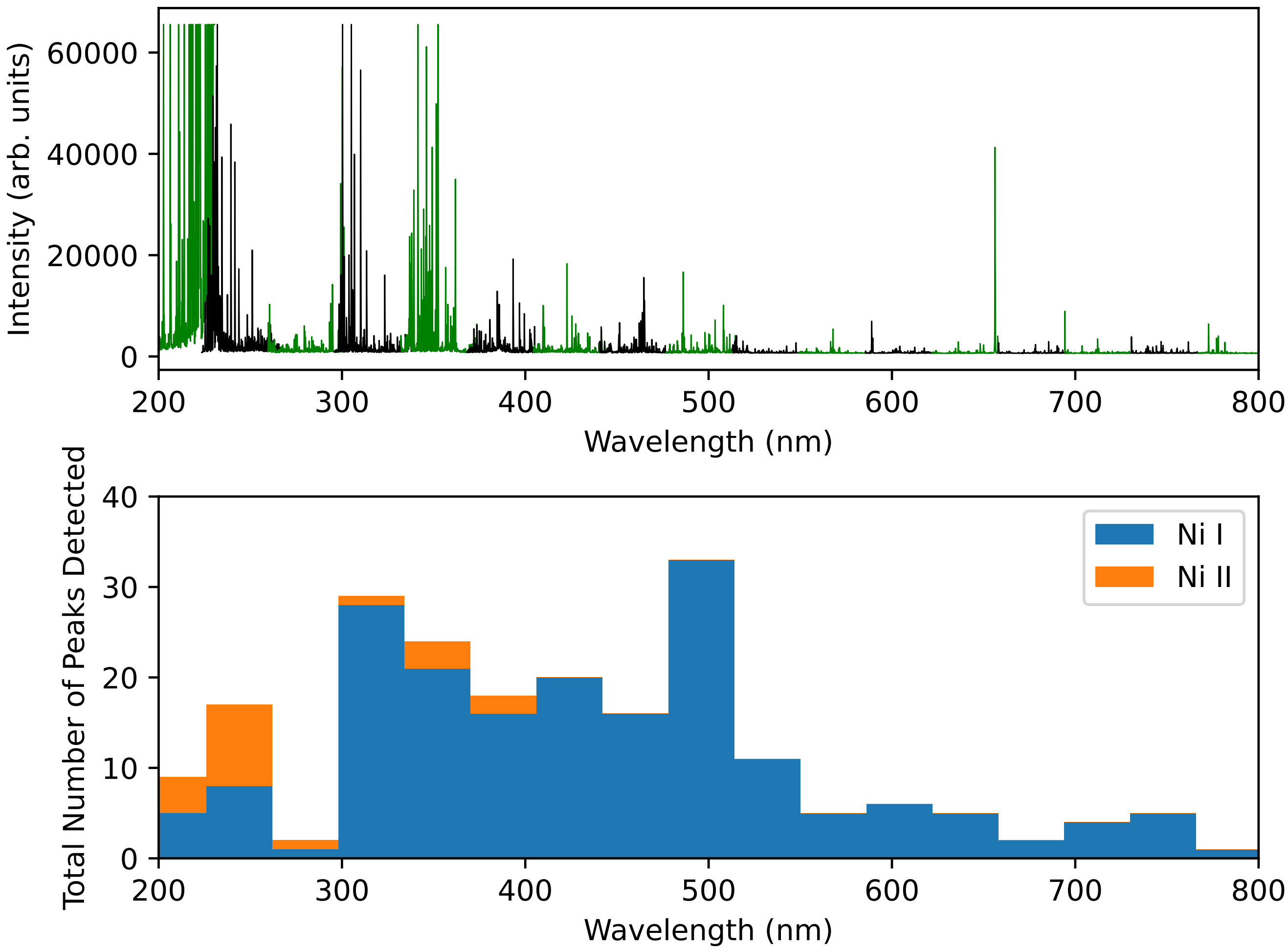

Figure 6. (Top) A stitched-together view of the Ni probe spectra from 200 - 800 nm at time $t = 42.5$ ms in each discharge. Windows are shown in alternating green/black for visibility. (Bottom) A histogram showing the number of Ni I (blue) and Ni II (orange) features detected in each wavelength window.

shown in red and newly-identified transitions shown in blue. The 13 low-lying levels of the configurations $3d^{10}$, $3d^9 4s$, and $3d^8 4s^2$ are metastable and could act as significant sources of population for the excited configurations $3d^9 4p$ and $3d^8 4s4p$. One may draw parallels to the structure of $5d$-shell elements. Many of the excited states of Ni I exhibit level purities of ∼30 - 80% (Kramida et al. 2020), owing to strong mixing following the breakdown of strong LS coupling. Similar mixing is observed in the lowest ion stages of gold (McCann et al. 2021). In cometary spectral models, metastable levels were required to accurately model the strengths of the lines emitted following decay of the excited odd-parity states (Bromley et al. 2021). Metastable-driven emission features were also identified in $5d$-shell spectral models of neutral gold (McCann et al. 2021). The majority of the newly-identified lines connect the highly-excited $3d^8 4s5s$ levels to the excited odd configurations $3d^8 4s4p$, and the excited even configurations $3d^9 nd$ and $3d^9 4s4d$ to the excited odd configuration $3d^8 4s4p$. At the electron temperatures present in CTH plasmas, it is likely that cascades also provide a non-negligible contribution to the strengths of the strongest emission lines, particularly from the excited even-parity states $3d^9 4s5s$ and $3d^9 4s4d$. These lines are likely sensitive to electron density and may be explored in future work as potential plasma diagnostics. We note that given the parities and energies of these highly excited states, direct excitation from the ground or metastable levels is likely weak. At present, the excitation source for these highly-excited transitions cannot be determined.

The electron temperature in CTH plasmas (∼ 30 eV) is sufficient to produce Ni II (ionization potential ∼ 7.6 eV), within the vicinity of the nickel probe. A Grotrian diagram of Ni II is shown in Fig. 5. A total of twenty transitions are shown, with newly-observed tran-

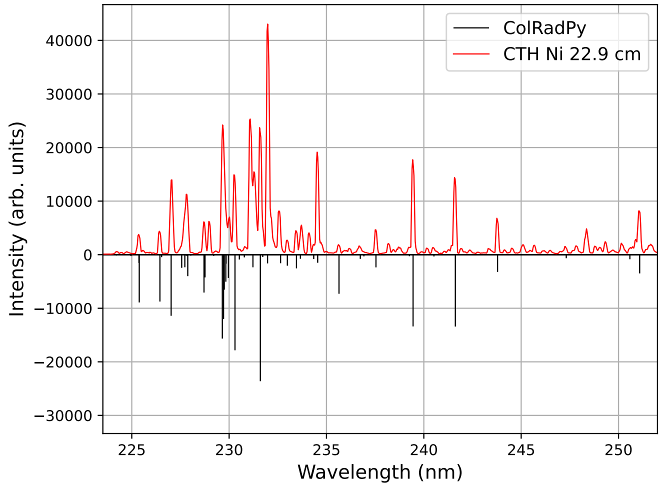

Figure 7. A comparison of CTH spectra (red) at t=36.25 ms to Ni II lines calculated using ColRadPy (black vertical lines). The CTH spectra were collected with the nickel probe 22.9 cm from the midplane of the CTH (shot #18112915). ColRadPy calculations assume an electron temperature of 30 eV and an electron density of $10^{12}\,\mathrm{cm}^{-3}$. The photon emissivity coefficients determined by ColRadPy are scaled to the CTH spectra and flipped below the x axis.

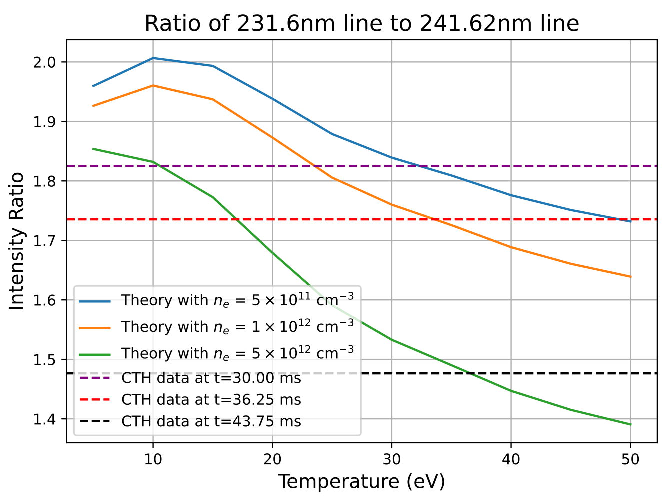

Figure 8. Ratio of 231.60 nm to 241.62 nm Ni II line intensities using CTH spectra (dashed lines) and calculated using ColRadPy (solid lines). Line intensities from the CTH spectra (shot #18112915) are found by fitting a Gaussian curve to each peak and calculating the integrated intensities.

sitions in blue. Many of the lines identified in this work were also identified by Clear et al. (2022), who analyzed spectra of a hollow cathode lamp with high-resolution Fourier transform spectroscopy. However, three lines are unreported in Clear et al. (2022). The three new lines are tentatively identified as $3d^84p \rightarrow 3d^84s$ transitions based on the Ritz wavelengths.

The number of observed Ni II lines is unexpectedly low when compared to Ni I. In contrast, previous experiments with gold probes showed considerable excitation of Au II. The relative lack of emission from Ni II in the Ni datasets are likely caused by several factors. First, the majority of the data were collected at 22.9 cm probe depth, which samples a cooler portion of the plasma edge. It is possible that the electron temperature and/or the electron density was insufficient to yield significant emission from Ni II, though this possibility is inconsistent with our explored emission models (discussed below). Second, the spectra collected at the 19.9 cm probe depth, which sampled an expectedly-higher temperature portion of the plasma, showed significant shot-to-shot variations and frequently 'disrupted' during the current-carrying portion of the discharge, resulting in a loss of confinement and a sudden decrease in probe erosion and Ni emission. Similar challenges were encountered in spectra collected at 16.9 cm probe depth in the previous gold campaign, which yielded disruptions in every 16.9 cm probe depth discharge.

Figure 3 shows the abundance of observed Ni I and Ni II lines in the observed wavelength ranges. While the Ni I emission exists throughout the UV-VIS region, the observed emission of Ni II is restricted primarily to the range 230 - 265 nm. The observed lines between 230 - 265 nm have lower levels which are metastable $3d^84s$ and have differing J values. In Ni II, twenty-one metastable states are lower in energy than the first excited odd parity state of $3d^84p$. The energies of these levels (~1 - 2 eV) and the energies of the odd-parity states gives rise to these close-lying lines, all of which are identified (based on their computed Ritz wavelengths) as $3d^8np \rightarrow 3d^8ns$ transitions. Given the complexity of the involved metastable levels and the close proximity in wavelength space, these lines are likely sensitive to both electron temperature and/or density.

4.1. *Benchmarking R-matrix data*

Dunleavy et al. (2021) recently calculated electron impact excitation collisional cross sections of Ni II using the R-matrix method. We utilize the results of these calculations as inputs for the collisional-radiative plasma emission modeling code ColRadPy (Johnson et al. 2019a). Figure 7 shows a comparison of CTH spectra to theoretical line intensities predicted by ColRadPy for an electron temperature of 30 eV and an electron density of $10^{12}\,\mathrm{cm}^{-3}$. Good agreement exists between the theoretical and experimental intensities for most lines. In order to benchmark theoretical lines, one would compare the relative intensities of lines in the experimental and theoretical results. Figure 8 shows an example of this process using the 231.57 and 241.62 nm Ni II lines. The blue and orange solid lines represent the ratio of the photon emissivity coefficients generated by the ColRadPy calculations run using electron temperatures from 5 eV to 50 eV at several different electron densities and, the dashed lines represent the intensity ratios from 3 different frames of the spectra collected during CTH plasmas. A precise measurement of the electron temperature was not acquired during this CTH experiment. However, because the electron temperature in the CTH changes as a function of time, the general trend of the line ratios as a function of changing plasma conditions can be observed from different exposures. The electron temperature in the CTH increases between 30 and 43.75 ms, while the intensity ratio of these two lines decreases, which is similar to the photon emissivity coefficient trend predicted by collisional-radiative modeling. It should be noted that there is a time-independent source of uncertainty in the line ratio measurements shown in Fig 8 arising from losses in the optical elements. Given that the lines used in Fig 8 are only 10 nm apart, we expect this effect to be relatively small. However, for the proposed benchmark line ratio studies, an intensity calibration should be performed. The photon emissivity coefficients are also strongly dependent on the Einstein A coefficients, and this relationship could be explored further in future investigations of CTH spectra. The agreement in these two figures demonstrates the feasibility of using CTH spectra to benchmark the accuracy of the R-matrix calculations.

To accurately benchmark theoretical data however, further CTH experiments would need to be conducted with localized measurements of the electron temperature throughout the experiment. Though a collisional-radiative analysis of the full Ni dataset is beyond the scope of this work, the authors note that access to the Ni spectra is available upon reasonable request for the purposes of benchmarking electron impact data.

5. CONCLUSION

The CTH experiment is demonstrated to be an advantageous platform for studying the emission of nickel as a significant number of new lines have been identified. These new Ni I and Ni II lines could be useful in future studies of solar nickel abundances as well as theoretical R-matrix or collisional-radiative calculations. Preliminary comparisons to R-matrix calculations have shown that CTH spectra could provide a useful benchmark if more precise electron temperature measurements are available. By comparing the relative intensities of two emission lines at different times during the plasma evolution, a significant change in their ratio is observed. Additionally, there is reasonable agreement between line intensity ratios and the photon emissivity ratios for expected electron temperatures. Furthermore, a comparison between the CTH spectra and theoretical spectra assuming similar plasma conditions agrees for most line intensities, which further supports the validity of this approach for benchmarking R-matrix calculations. CTH experiments are particularly useful for detecting transitions from high energy levels due to the high electron temperature achieved ($\sim$30 eV) during current-carrying plasmas. By comparing spectra acquired from probes of various elements to measurements with a nickel probe, background lines can be distinguished from purely nickel emission lines. The technique described here can be applied to many other elements as well. In combination with previous experiments, it could provide useful benchmarks for future atomic structure calculations as well as a more thorough understanding of the nickel emission spectra to be used in astrophysical applications.

6. ACKNOWLEDGEMENTS

The authors gratefully acknowledge funding support from the Clemson University College of Science, the National Science Foundation (Grants #1815833, #1815932, #1816984) and the US Department of Energy (Grants #DE-FG02-00ER54610 and #DE-SC0015877). The authors also thank Connor Ballance for his contributions to the comparisons with theoretical R-matrix calculations.

REFERENCES

Asplund, M., Grevesse, N., Sauval, A. J., & Scott, P. 2009, ARA&A, 47, 481, doi: 10.1146/annurev.astro.46.060407.145222

Bell, G. D., Paquette, D. R., & Wiese, W. L. 1966, ApJ, 143, 559, doi: 10.1086/148534

Bromley, S., Neff, B., Loch, S., et al. 2021, Atomic iron and nickel in the coma of C/1996 B2 (Hyakutake): production rates, emission mechanisms, and possible parents. https://arxiv.org/abs/2106.04701

Bromley, S. J., Johnson, C. A., Ennis, D. A., et al. 2020, 250, 19, doi: 10.3847/1538-4365/abaa4d

Clear, C. P., Pickering, J. C., Nave, G., Uylings, P., & Raassen, T. 2022, The Astrophysical Journal Supplement Series, 261, 35, doi: 10.3847/1538-4365/ac7f9b

Doerr, A., & Kock, M. 1985, Journal of Quantitative Spectroscopy & Radiative Transfer, 33, 307

Dunleavy, N. L., Ramsbottom, C. A., & Ballance, C. P. 2021, A&A, 648, A67, doi: 10.1051/0004-6361/202038254

Grevesse, N., & Swings, J. 1970, Solar Physics, 13, 19, doi: 10.1007/BF00963938

Hartwell, G. J., Knowlton, S. F., Hanson, J. D., Ennis, D. A., & Maurer, D. A. 2017, Fusion Science and Technology, 72, 76, doi: 10.1080/15361055.2017.1291046

Huber, M. C. E., & Sandeman, R. J. 1980, A&A, 86, 95

Johnson, C. A. 2020, PhD thesis, Auburn University. https://etd.auburn.edu//handle/10415/7551

Johnson, C. A., Ennis, D. A., Loch, S. D., & Ballance, C. P. 2023, Nuclear Fusion, 63, 096017, doi: 10.1088/1741-4326/ace3d9

Johnson, C. A., Loch, S. D., & Ennis, D. A. 2019a, Nuclear Materials and Energy, 20, 100579, doi: https://doi.org/10.1016/j.nme.2019.01.013

Johnson, C. A., Ennis, D. A., Loch, S. D., et al. 2019b, 61, 095006, doi: 10.1088/1361-6587/ab2b25

Kostyk, R. I. 1982, Astrometriia i Astrofizika, 46, 58

Kramida, A., Yu. Ralchenko, Reader, J., & and NIST ASD Team. 2020, NIST Atomic Spectra Database (ver. 5.8), [Online]. Available: `https://physics.nist.gov/asd` [2016, January 31]. National Institute of Standards and Technology, Gaithersburg, MD.

Lennard, W. N., Whaling, W., Scalo, J. M., & Testerman, L. 1975, ApJ, 197, 517, doi: 10.1086/153538

McCann, M., Bromley, S., Loch, S. D., & Ballance, C. P. 2021, Monthly Notices of the Royal Astronomical Society, 509, 4723, doi: 10.1093/mnras/stab3285

Meggers, W. F., Corliss, C. H., & Scribner, B. F. 1975, National Bureau of Standards Monograph, doi: 10.6028/NBS.MONO.145p1

Meggers, W. F., & Kiess, C. C. 1919, 14, 637, doi: https://dx.doi.org/10.6028/bulletin.352

Morton, D. C. 2000, The Astrophysical Journal Supplement Series, 130, 403, doi: 10.1086/317349

Shenstone, A. G. 1970, J Res Natl Bur Stand A Phys Chem, 74A, 801

Wickliffe, M. E., & Lawler, J. E. 1997, 110, 163, doi: 10.1086/312995

Table 2. Observed Transitions of Ni I.

λ_{obs}	λ_{Ritz}	λ_{diff}	Intensity	E_{lower}	E_{upper}	Lower Index	Upper Index	References
205.29	205.25	-0.04	2	1332.164	50039.191	3	100	1
210.87*	210.9	0.03	66	1332.164	48735.29	3	83	
211.42	211.45	0.03	49	3409.937	50689.489	6	109	1
219.09	219.13	0.04	22	3409.937	49032.926	6	86	1
223.1	223.1	0	100	1713.087	46522.866	4	73	1
229.33	229.32	-0.01	31	879.816	44475.099	2	68	1
232.57	232.59	0.02	49	1332.164	44314.904	3	59	1
232.99	233	0.01	16	2216.55	45122.383	5	70	1
233.72*	233.72	0	27	879.816	43654.974	2	61	
234.53	234.55	0.02	100	0	42620.994	0	55	1, 2
245.09*	245.05	-0.04	14	3409.937	44206.099	6	64	
247.63	247.65	0.02	4	2216.55	42585.212	5	53	1, 2
252.47*	252.43	-0.04	16	879.816	40484.212	2	52	
282.09	282.13	0.04	56	204.787	35639.122	1	49	1, 2, 3
298.13	298.17	0.04	100	879.816	34408.555	2	48	2
301.23	301.2	-0.03	22	3409.937	36600.791	6	50	1, 2, 3
301.93	301.92	-0.01	3	0	33112.334	0	43	2,3
303.82	303.8	-0.02	26	204.787	33112.334	1	43	2, 3
304.48	304.5	0.02	1	1332.164	34163.264	3	47	2,3
305.1	305.09	-0.01	100	204.787	32973.376	1	41	2,3
305.81	305.77	-0.04	17	1713.087	34408.555	4	48	2, 3
306.43	306.47	0.04	13	879.816	33500.822	2	44	2, 3
308.11	308.08	-0.03	4	1713.087	34163.264	4	47	1, 2, 3
309.92	309.91	-0.01	2	1332.164	33590.13	3	45	2, 3
310.17	310.16	-0.01	76	879.816	33112.334	2	43	2, 3
310.54*	310.55	0.01	1	2216.55	34408.555	5	48	
312.96	312.93	-0.03	1	2216.55	34163.264	5	47	3
316.35*	316.38	0.03	1	15609.844	47208.149	9	76	
318.2*	318.18	-0.02	1	15609.844	47030.102	9	74	
318.62*	318.65	0.03	1	2216.55	33590.13	5	45	
320.01*	320.05	0.04	6	204.787	31441.635	1	39	
322.16	322.17	0.01	2	0	31031.02	0	38	1,2,3
322.35*	322.37	0.02	1	26665.887	57677.575	14	132	
323.32	323.3	-0.02	25	0	30922.734	0	36	1,2,3
324.33	324.31	-0.02	3	204.787	31031.02	1	38	1, 2, 3
325.1	325.08	-0.02	1	3409.937	34163.264	6	47	2, 3
327.13	327.11	-0.02	1	879.816	31441.635	2	39	1, 2, 3
328.46*	328.45	-0.01	1	26665.887	57103.88	14	131	
331.24*	331.25	0.01	2	3409.937	33590.13	6	45	
331.57	331.57	0	3	879.816	31031.02	2	38	1, 2
332.01	332.03	0.02	1	1332.164	31441.635	3	39	1, 2, 3
332.21	332.23	0.02	5	3409.937	33500.822	6	44	2, 3
336.12*	336.08	-0.04	6	14728.84	44475.099	8	68	
336.54	336.58	0.04	3	3409.937	33112.334	6	43	2, 3
336.95	336.96	0.01	29	0	29668.918	0	28	1, 2, 3
337.16	337.2	0.04	31	1332.164	30979.749	3	37	1, 2
338.01*	337.97	-0.04	100	1332.164	30912.817	3	35	

342.31*	342.32	0.01	30	14728.84	43933.408	8	62	
343.95*	344.02	0.07	2	1332.164	30392.003	3	33	
345.79*	345.78	-0.01	83	27260.894	56172.657	15	127	
346.93*	346.95	0.02	5	2216.55	31031.02	5	38	
350.04	350.02	-0.02	19	28542.105	57103.88	20	131	1, 2, 3
352.8	352.8	0	5	1332.164	29668.918	3	28	2, 3
354.41*	354.45	0.04	5	879.816	29084.456	2	24	
355.12	355.16	0.04	4	1332.164	29480.989	3	26	2, 4
355.72*	355.72	0	0	28068.065	56172.657	19	127	
356.57*	356.55	-0.02	68	14728.84	42767.853	8	57	
357.12*	357.09	-0.03	33	27580.391	55576.843	17	126	
357.57*	357.61	0.04	3	1713.087	29668.918	4	28	
360.97*	360.93	-0.04	42	879.816	28578.018	2	22	
362.18*	362.17	-0.01	2	28569.203	56172.657	21	127	
362.4*	362.41	0.01	10	26665.887	54251.308	14	125	
367.32*	367.34	0.02	4	29888.477	57103.88	30	131	
373.89	373.93	0.04	16	1332.164	28068.065	3	19	1,2
376.21*	376.2	-0.01	5	30192.251	56766.48	32	129	
377.54	377.56	0.02	29	3409.937	29888.477	6	30	1, 2
378.35	378.36	0.01	38	3409.937	29832.779	6	29	1, 2
379.2	379.24	0.04	27	2216.55	28578.018	5	22	3
380.7	380.72	0.02	73	3409.937	29668.918	6	28	1
381.12*	381.13	0.01	3	1713.087	27943.524	4	18	
381.88*	381.85	-0.03	2	30922.734	57103.88	36	131	
383.17	383.17	0	18	3409.937	29500.674	6	27	1, 2
385.83	385.83	0	100	3409.937	29320.762	6	25	1, 2
386.83*	386.83	0	10	30922.734	56766.48	36	129	
387.65*	387.69	0.04	8	30979.749	56766.48	37	129	
388.96*	388.94	-0.02	34	25753.553	51457.25	13	121	
394.85*	394.87	0.02	3	31786.162	57103.88	40	131	
395.75*	395.78	0.03	4	30912.817	56172.657	35	127	
402.78	402.77	-0.01	3	31441.635	56262.913	39	128	5
412.22*	412.19	-0.03	6	27943.524	52197.444	18	123	
413.17*	413.17	0	44	27260.894	51457.25	15	121	
415.67*	415.67	0	1	26665.887	50716.896	14	111	
415.78*	415.82	0.04	15	27414.868	51457.25	16	121	
420.05	420.05	0	46	26665.887	50466.131	14	106	5
420.21*	420.17	-0.04	42	32973.376	56766.48	41	129	
423.14*	423.11	-0.03	28	28569.203	52197.444	21	123	
425.97*	425.93	-0.04	39	28569.203	52040.523	21	122	
427.95*	427.92	-0.03	85	27943.524	51306.038	18	119	
428.31*	428.34	0.03	12	27414.868	50754.103	16	113	
428.82*	428.8	-0.02	58	30922.734	54237.099	36	124	
429.59	429.59	0	19	30979.749	54251.308	37	125	4
430.25*	430.21	-0.04	20	28068.065	51306.038	19	119	
431.34*	431.36	0.02	9	33590.13	56766.48	45	129	
432.31*	432.3	-0.01	14	27580.391	50706.273	17	110	
433.14*	433.17	0.03	49	13521.347	36600.791	7	50	
435.48*	435.49	0.01	12	27580.391	50536.703	17	107	
436.96*	436.96	0	9	28578.018	51457.25	22	121	

440.16	440.16	0	100	25753.553	48466.49	13	80	2, 4
441.09*	441.05	-0.04	33	26665.887	49332.593	14	97	
444.94*	444.94	0	37	28068.065	50536.703	19	107	
451.79*	451.79	0	47	28578.018	50706.273	22	110	
454.66*	454.69	0.03	27	33590.13	55576.843	45	126	
456.11*	456.13	0.02	11	27414.868	49332.593	16	97	
456.75	456.74	-0.01	23	28578.018	50466.131	22	106	5
459.98*	459.98	0	26	28542.105	50276.321	20	103	
466.71*	466.7	-0.01	7	30619.414	52040.523	34	122	
467.42*	467.4	-0.02	47	27943.524	49332.593	18	97	
467.55	467.56	0.01	39	29084.456	50466.131	24	106	5
468.19*	468.18	-0.01	25	29480.989	50834.401	26	116	
470.1*	470.13	0.03	56	30192.251	51457.25	32	121	
471.39*	471.38	-0.01	100	28569.203	49777.569	21	99	
473.19	473.18	-0.01	45	30912.817	52040.523	35	122	5
474.99*	474.97	-0.02	26	29668.918	50716.896	28	111	
476.33*	476.35	0.02	69	22102.325	43089.578	12	59	
477.28*	477.29	0.01	13	29888.477	50834.401	30	116	
478.59	478.63	0.04	33	13521.347	34408.555	7	48	3
479.72*	479.76	0.04	9	30619.414	51457.25	34	121	
480.72	480.7	-0.02	15	29668.918	50466.131	28	106	2, 5
481.62*	481.6	-0.02	1	28569.203	49327.811	21	95	
483.91*	483.87	-0.04	6	33590.13	54251.308	45	125	
484.3	484.32	0.02	5	13521.347	34163.264	7	47	4
485.27	485.26	-0.01	4	28569.203	49171.151	21	90	5
487.11*	487.08	-0.03	3	30192.251	50716.896	32	111	
487.38*	487.35	-0.03	6	29832.779	50346.427	29	104	
491.18	491.2	0.02	4	30392.003	50744.552	33	112	5
491.4	491.4	0	7	30192.251	50536.703	32	107	5
491.87*	491.84	-0.03	11	30979.749	51306.038	37	119	
492.11*	492.12	0.01	1	29013.206	49327.811	23	95	
492.46*	492.46	0	6	29013.206	49313.814	23	94	
493.73	493.74	0.01	28	29084.456	49332.593	24	97	5
495.32*	495.32	0	4	30163.124	50346.427	31	104	
497.14*	497.16	0.02	7	29668.918	49777.569	28	99	
498.02	498.02	0	44	29084.456	49158.48	24	88	2, 4
498.42*	498.41	-0.01	15	30619.414	50677.555	34	108	
499.66	499.69	0.03	2	29320.762	49327.811	25	95	5
503.55	503.54	-0.01	53	29320.762	49174.77	25	91	2, 5
503.9	503.94	0.04	11	29320.762	49159.03	25	89	4
504.86	504.89	0.03	12	31031.02	50832.001	38	115	2, 5
505.15*	505.15	0	9	29480.989	49271.54	26	93	
505.62*	505.66	0.04	8	29500.674	49271.54	27	93	
508.07	508.05	-0.02	100	29480.989	49158.48	26	88	2, 4
508.41	508.41	0	51	29668.918	49332.593	28	97	2, 5
508.87*	508.86	-0.01	5	31031.02	50677.555	38	108	
509.44	509.44	0	3	30912.817	50536.703	35	107	5
509.98	510	0.02	33	29668.918	49271.54	28	93	2, 5
510.46*	510.45	-0.01	2	29500.674	49085.982	27	87	
511.53	511.54	0.01	38	30922.734	50466.131	36	106	5

512.9	512.94	0.04	14	29668.918	49159.03	28	89	2, 4
516.84*	516.87	0.03	60	29832.779	49174.77	29	91	
517.65	517.66	0.01	24	31441.635	50754.103	39	113	2, 5
518.46*	518.46	0	26	29888.477	49171.151	30	90	
523.81*	523.82	0.01	6	33112.334	52197.444	43	123	
525.97*	525.95	-0.02	7	30163.124	49171.151	31	90	
532.07*	532.05	-0.02	10	30163.124	48953.316	31	85	
541.1*	541.12	0.02	12	32982.26	51457.25	42	121	
545.34	545.32	-0.02	8	32973.376	51306.038	41	119	5
546.22	546.25	0.03	29	31031.02	49332.593	38	97	5
547.66	547.69	0.03	100	14728.84	32982.26	8	42	2, 3
549.9*	549.93	0.03	16	30979.749	49159.03	37	89	
550.98*	550.94	-0.04	15	16017.306	34163.264	11	47	
564.7*	564.68	-0.02		32973.376	50677.555	41	108	
568.09*	568.13	0.04	100	26665.887	44262.599	14	65	
571.8*	571.8	0	70	32982.26	50466.131	42	106	
581.09*	581.05	-0.04	50	33500.822	50706.273	44	110	
600.69*	600.73	0.04	2	13521.347	30163.124	7	31	
608.768*	608.72	-0.04	10	34408.555	50832.001	48	115	
611.08	611.11	0.03	32	32973.376	49332.593	41	97	5
616.52*	616.53	0.01	13	33112.334	49327.811	43	95	
617.62*	617.66	0.04	100	32973.376	49159.03	41	89	
620.46	620.46	0	32	32973.376	49085.982	41	87	5
622.38*	622.4	0.02	23	33112.334	49174.77	43	91	
623*	623.01	0.01	46	33112.334	49159.03	43	89	
631.45	631.47	0.02	100	15609.844	31441.635	9	39	2, 4
642.12	642.15	0.03	40	33590.13	49158.48	45	88	4
650.77*	650.73	-0.04	88	33590.13	48953.316	45	85	
663.08*	663.05	-0.03	31	35639.122	50716.896	49	111	
693.18*	693.19	0.01	100	13521.347	27943.524	7	18	
703.21*	703.22	0.01	12	42585.212	56801.586	53	130	
712.2	712.22	0.02	100	28569.203	42605.945	21	54	2, 5
718.16*	718.2	0.04	6	30192.251	44112.173	32	63	
723.61*	723.63	0.02	16	16017.306	29832.779	11	29	
738.23	738.19	-0.04	19	43258.726	56801.586	60	130	5
740.96*	740.93	-0.03	22	30619.414	44112.173	34	63	
752.53*	752.51	-0.02	36	29320.762	42605.945	25	54	
755.58*	755.56	-0.02	38	31031.02	44262.599	38	65	
761.7	761.7	0	100	29480.989	42605.945	26	54	2
771.55*	771.56	0.01	100	29832.779	42790.01	29	58	
771.54*	771.56	-0.02	100	29832.779	42790.01	29	58	

Notes. Wavelengths are reported in nm and energies are given in cm^{-1}. An asterisk next to the experimental wavelength denotes a line that has not previously been observed. The intensity listed is the integrated line intensity for one exposure, which is then normalized such that the strongest line in each wavelength range has an intensity of 100. Horizontal lines show the cutoff between different wavelength ranges. Comparisons of line intensities should not be made between lines that fall into different wavelength ranges. The upper and lower index can be used to find more information about the upper and lower energy levels using the tables provided in the supplementary materials. Energy level data is taken from the NIST Atomic Spectra Database (Kramida et al. 2020). The Ritz wavelength in air is calculated using these energy levels.

References. (1) Huber & Sandeman (1980); (2) Meggers et al. (1975); (3) Doerr & Kock (1985); (4) Lennard et al. (1975); (5) Kostyk (1982)

Table 3. Observed Transitions of Ni II

λ_{obs}	λ_{Ritz}	λ_{diff}	Intensity	E_{lower}	E_{upper}	Lower Index	Upper Index	References
203.37	203.35	-0.02	1	9330.04	58493.21	3	33	1,3
212.59	212.6	0.01	3	8393.9	55417.83	2	27	1,3
222.53	222.49	-0.04	100	9330.04	54262.63	3	23	1,3
225.43	225.39	-0.04	71	10663.89	55018.71	5	25	1,2,3
231.6	231.61	0.01	100	8393.9	51557.85	2	17	1,2,3
235.63	235.65	0.02	8	14995.57	57420.16	7	32	1,3
237.53	237.55	0.02	17	14995.57	57080.55	7	31	1,2,3
239.44	239.46	0.02	68	13550.39	55299.65	6	26	1,2,3
241.27	241.23	-0.04	2	10115.66	51557.85	4	17	1,3
241.59	241.62	0.03	57	14995.57	56371.41	7	29	1,2,3
243.35	243.36	0.01	5	14995.57	56075.26	7	28	1,3
251.05	251.09	0.04	0	13550.39	53365.17	6	19	1,2,3
254.57	254.6	0.03	8	14995.57	54262.63	7	23	1,3
264.9	264.88	-0.02	2	14995.57	52738.45	7	18	3
303.24*	303.25	0.01	100	23108.28	56075.26	8	28	
335.06	335.05	-0.01	62	23796.18	53634.62	9	21	3
342.05*	342.06	0.01	86	25036.38	54262.63	12	23	
345.44	345.42	-0.02	74	23796.18	52738.45	9	18	3
372.56*	372.6	0.04	100	29593.46	56424.49	14	30	
376.91	376.95	0.04	45	25036.38	51557.85	12	17	3

Notes. Wavelengths are given in nm and energies are given in cm^{-1}. An asterisk next to the experimental wavelength denotes a line that has not previously been observed. The intensity listed is the integrated line intensity for one exposure, which is then normalized such that the strongest line in each wavelength range has an intensity of 100. Horizontal lines show the cutoff between different wavelength ranges. Comparisons of line intensities should not be made between lines that fall into the different wavelength ranges. The upper and lower index can be used to find more information about the upper and lower energy levels in the tables provided in the supplementary materials. Energy level data is taken from the NIST Atomic Spectra Database (Kramida et al. 2020). The Ritz wavelength in air is calculated using these energy levels.

References. (1) Bell et al. (1966); (2) Shenstone (1970); (3) Clear et al. (2022)